Structural disorder and antiferromagnetism in $LaNi_{1-x}Pt_xO_3$

A. S. Fjellvåg[a]*, Ø. S. Fjellvåg[b], Y. Breard[c], and A. O. Sjåstad[a]*

[a]Department of Chemistry, Centre for Materials Science and Nanotechnology, University of Oslo, Norway

[b]Department for Neutron Materials Characterization, Institute for Energy Technology, PO Box 40, NO-2027, Kjeller, Norway

[c]Laboratoire CRISMAT, UMR 6508 CNRS ENSICAEN, 6 bd du Maréchal Juin, 14050 Caen Cedex 4, France

*a.o.sjastad@kjemi.uio.no; a.s.fjellvag@smn.uio.no

1. Abstract

We report on the *B*-site substitution of Pt for Ni in the system $LaNi_{1-x}Pt_xO_3$. The system can only be synthesized between $x \leq 0.50$, with $LaNiO_3$ ($x = 0.00$) and the stoichiometric double perovskite La_2NiPtO_6 ($x = 0.50$) as the end members. Higher Pt-contents ($x > 0.50$) are unachievable due to the preference of Pt to being in oxidation state +IV in octahedral coordination. Upon introducing Pt into $LaNiO_3$, a phase transformation from rhombohedral (*R*-*3c*) to monoclinic ($P2_1/n$) symmetry is observed for $0.075 \leq x \leq 0.125$, where all monoclinic samples are *B*-site ordered, and Pt show a strong preference for the Pt-site (2*c*-site) for all compositions ($x \geq 0.20$). Powder X-ray diffraction analysis reveal disorder of the Pt-distribution in several of the samples with a non-equimolar Ni/Pt ratio ($0.20 \leq x \leq 0.40$), which point toward cluster formation with domains of high and low Pt-content within each sample. La_2NiPtO_6 further show an antiferromagnetic transition at ~40 K. A similar transition is observed for all monoclinic samples ($x \geq 0.20$), however, the transition becomes less pronounced for lower *x*. This is explained in terms of the structural disorder, *i.e.* by the coexistence of antiferromagnetic domains with long range order and paramagnetic domains dominated by short range antiferromagnetic interactions.

2. Introduction

Platinum, one of the most stable noble metals, has been utilized for applications for centuries, *e.g.* in crucibles for high temperature heat treatments and in thermocouples. This has led to the discovery of several different Pt containing oxides [1], through unexpected side reactions. Pt has preference for oxidation state 0, +II and +IV, as seen from the stability of Pt metal at low partial pressures of oxygen (pO_2), Pt_3O_4 at intermediate temperature and pO_2, and PtO_2 at higher pO_2 [1]. The stability of the +II and +IV states of Pt can be rationalized by the square planar coordination with a d^8-configuration (+II) and an octahedral coordination with a d^6 low spin configuration (+IV).

In double perovskites, such as La_2CoPtO_6, Pt adopts the +IV oxidation state. The compound is insulating and weakly ferromagnetic at low temperature ($T < \sim 50$ K) [2]. Compared with La_2CoIrO_6, the magnetic interaction between Co(II, high spin) and Pt(IV) is weak [2], explained through a hybridization mechanism first applied on Cr-based double perovskites [3]. In these 5*d*-systems, spin orbit coupling may also affect the magnetic interactions. The synthesis procedure for the similar compound, La_2NiPtO_6, has previously been reported [4], but its magnetic properties are so far unrevealed. Additionally, neither $LaCo_{1-x}Pt_xO_3$ nor $LaNi_{1-x}Pt_xO_3$ have been tried synthesized and investigated for non-equimolar compositions ($x \neq 0.50$).

It is well-known that $LaNiO_3$ is a Pauli paramagnetic metal, which upon *B*-site substitution turn insulating. The magnetic properties of $LaNiO_3$ are highly dependent on structural distortions induced by substitution, the choice of substituent element, and the consecutive internal redox processes; the result is varying ferro- (FM) and antiferromagnetic (AFM) interactions [5-10]. In Sr_2FeMoO_6, the grain structure and degree of *B*-site ordering has been shown to strongly influence both magnetoresistance and magnetic properties [11, 12], also for non-equimolar compositions [13]. By applying various synthesis protocols, different degree of long range Fe-Mo ordering can be achieved. However, the short range Fe-Mo ordering is still present, regardless of the degree of long range ordering. For *B*-site substituted $LaNiO_3$, long range ordering is only achieved by substitution with 4*d*- or 5*d*-elements which obtain a +IV oxidation state, reducing Ni to +II [14]. The subsequent order-disorder phenomena and the effect on magnetic properties in $LaNiO_3$, in both equimolar and non-equimolar compositions, has so far attracted little attention.

Herein we investigate the structure and magnetic properties of $LaNi_{1-x}Pt_xO_3$, $0 \leq x \leq 0.50$. Inspired by the studies on Sr_2FeMoO_6, we pay special attention to the structural disorder of non-equimolar compounds in the system $LaNi_{1-x}Pt_xO_3$. We further evaluate magnetic properties below room temperature, and correlate low temperature magnetic ordering to structural disorder.

3. Experimental

$La(NO_3)_3 \times 6H_2O$ (99.9 %) and $Ni(NO_3)_2 \times 6H_2O$ (99 %) were purchased from Alfa and KEBO Lab, respectively, whereas Pt metal (99.9 %) was purchased from Heraeus and citric acid ($C_6O_7H_8 \times H_2O$; 98 %) was purchased from Sigma-Aldrich. The La and Ni nitrate salts were dissolved in water and the accurate salt concentrations (mol/g) of the solutions were determined by thermogravimetry. All samples were synthesized using a citric acid complexation method. Stoichiometric amounts of La- and Ni nitrate solutions and Pt metal were weighed out, before the Pt metal was dissolved in aqua regia (1 part HNO_3, 3 parts HCl, VWR Chemicals). The two solutions were mixed, and 50 g of citric acid was added per gram of targeted oxide product. The solution was boiled until complete loss of water and nitrate in form of nitrous gasses, followed by overnight heat treatment at 180 °C. The samples were subsequently calcined at 400 °C in air for 12 hours before pelletizing and high temperature heat treatment. For the first annealing step, samples with $x \geq 0.30$ were annealed at 1000 °C in sealed quartz ampoules with 7 bar O_2 for 12 hours, using Ag_2O (KEBO Lab, 99 %) as the oxidizing agent, which releases O_2 during the heating sequence whereas samples with $x \leqslant 0.25$ were annealed at 850 °C in a

flow of O_2 (from AGA, 5.0 quality) for 12 hours. In the second annealing step, all samples were annealed at 1000 °C for 12 hours in a flow of O_2. For $LaNiO_3$ ($x = 0$), the high temperature heat treatment was performed twice at 850 °C in a flow of O_2 for 48 hours. The synthesis conditions are expected to provide O-content near 3.0 in $LaNiO_3$ [15]. Prior to the magnetic measurements, samples with compositions $x = 0.20$, $x = 0.30$ and $x = 0.40$ where annealed again for 2 weeks at 1000 °C in a flow of O_2, in order to improve the homogeneity of the samples.

Powder X-ray diffraction (XRD) were performed for all samples in the home laboratory using a Siemens Bruker-AXS D5000 diffractometer with Cu Kα1 radiation (λ = 1.5406 Å) and transmission flat-plate geometry. Powder synchrotron X-ray diffraction data for selected samples (x = 0.00, 0.05, 0.20, 0.30, 0.40, 0.50) were collected at beam line BM01B at the Swiss-Norwegian Beam Lines (SNBL), European Synchrotron Radiation Facility (ESRF) in Grenoble, France [16]. Synchrotron XRD experiments were performed using a 2D Dexela detector and wavelength λ = 0.50506 Å for x = 0.00, λ = 0.50467 Å for x = 0.05, x = 0.20, x = 0.30 and x = 0.40, while for x = 0.50, a high-resolution detector with six Si(111) analyzer crystals and λ = 0.50506 Å was used. The data was collected after the initial 2×12 hours heat treatment. The x = 0.50 sample was mixed with MgO to reduce absorption. One additional dataset (Figure S5b) of synchrotron XRD of $LaNi_{0.70}Pt_{0.30}O_3$ were collected after the sample were annealed for two additional weeks. The data were collected at BM01, SNBL (ESRF), using λ = 0.71490 Å and a PILATUS 2M detector. Obtained data were reduced with the Bubble software [17], and the 2D diffraction patterns were visualized with the ALBULA software. Structural analysis was performed by Rietveld refinements using the software TOPAS [18]. For all datasets, we refined scale factor, background polynomial, Gaussian and Lorentzian peak shape and zero error. For the structures, the lattice parameters, atomic positions, thermal displacement factors and occupancies were refined. The occupancies of Ni(II), Ni(III) and Pt(IV) were restricted to yield charge neutrality and the nominal composition in total for all refinements. Identical atomic positions were used in the refinements for both structures in the two-phase (domain) model, while the scale factor, lattice parameters and peak profile was refined individually.

Magnetic measurements were performed using a Quantum Design physical properties measurement system (QD-PPMS). Samples for DC magnetization were measured from 4 to 300 K using a 2000 Oe external DC-field. In AC magnetization mode, samples were measured from 4 to 60 K both with and without a 2000 Oe external DC field, and with a 10 and 15 Oe AC field with frequencies of 117, 1117, 1997, 4997 and 9997 Hz. Field dependent DC magnetization measurements were performed at 4 K with a DC field variating between –9 and 9 Tesla.

4. Results

4.1 Synthesis and phase relations

In this work, we have investigated $LaNiO_3$, La_2NiPtO_6 and $LaNi_{1-x}Pt_xO_3$ for $0 \leq x \leq 0.70$. $LaNiO_3$ is a rhombohedral (*R-3c*) perovskite (Figure 1a), while La_2NiPtO_6 is a monoclinic (*P2₁/n*) double perovskite with *B*-site ordering and a β-angle very close to 90° (Figure 1b).

Attempts to synthesize Pt containing samples by a solid-state route using Pt metal as precursor proved unsuccessful, as the metallic Pt did not oxidize completely, and Pt metal impurities were present in the products. As an alternative, we turned to the citric acid complexation synthesis route, where the precursor elements are mixed in a solution to ensure good atomic distribution. Combined with a high pO_2 during annealing, we avoid that platinum nucleates to Pt metal particles during synthesis. Correspondingly, we find all samples in the range $0 \leq x \leq 0.40$ to be phase pure (Figure S1), while for x = 0.50, < 0.50 mol % Pt is present. For x = 0.60 and x = 0.70, La_2NiPtO_6 is formed, in addition to significant quantities of Pt and La_2O_3 impurities. We believe a higher Pt-content than x = 0.50 cannot be stabilized in this system since Pt is unable to adopt lower oxidations states than +IV in the perovskite, and Ni will not go below +II under regular synthesis conditions.

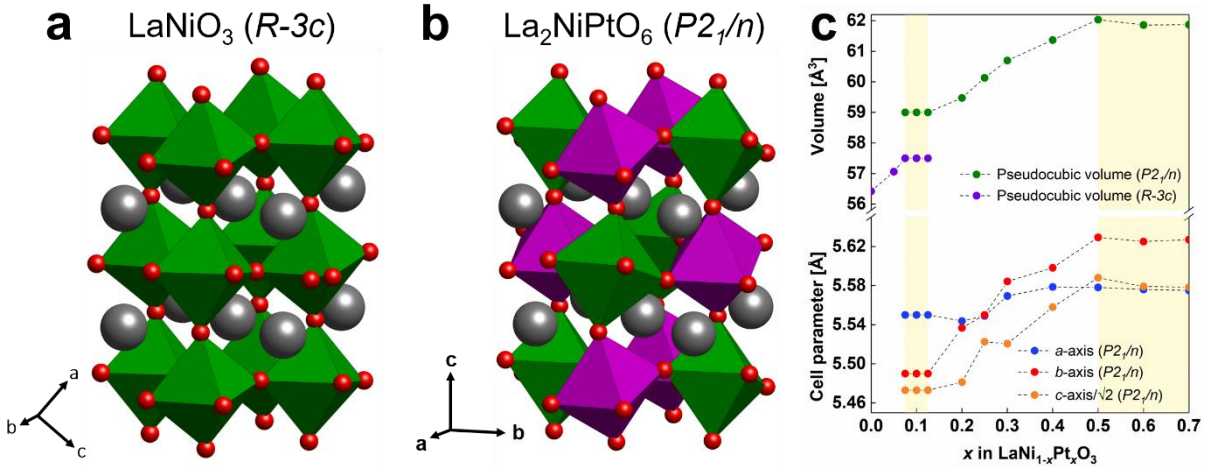

Figure 1: Crystal structure of (a) $LaNiO_3$ (*R-3c*) and (b) La_2NiPtO_6 (*P2₁/n*). (c) Cell parameters and pseudocubic cell volume for the $LaNi_{1-x}Pt_xO_3$ system, where the *c*-axis of the monoclinic phase is divided by √2 for direct comparison. The rhombohedral lattice parameters (low *x*) are excluded for clarity (Figure S2). The white areas are compositions with single phase, while for the beige areas, multiple phases are present.

Upon the introduction of Pt into $LaNiO_3$, forming $LaNi_{1-x}Pt_xO_3$, a phase transformation from *R-3c* to *P2₁/n* occurs, and a structural two-phase region is observed for $0.075 \leq x \leq 0.125$ (Figure 1c). This imply that only a small solid solution range is associated with Pt-substitution for Ni (6*b*-site, Table S1) in $LaNiO_3$, without causing a phase transformation. However, a much larger substitutional range is possible with Ni-substitution for Pt (2*c*-site, Table S2) in La_2NiPtO_6, as in $La_2Ni_{2-2x}Pt_{2x}O_6$ ($0.20 \leq x \leq 0.50$). At the phase boundary, the unit cell volume of the monoclinic phase is ~2.6 % larger than the rhombohedral phase (Figure 1c). Comparing the cell parameters of the monoclinic cell (*c*-axis is divided by $\sqrt{2}$), we observe that the three axis lengths become very similar ($a \approx b \approx c/\sqrt{2}$) (Figure 1c), *i.e.* there is no strong anisotropic distortion induced by the Pt-substitution. In addition, we note the trend of expansion for the unit cell parameters and volume (Figure 1c) with increasing Pt content (x). When entering the regime $x \geq 0.50$, the unit cell parameters and volume flatten out, consistent with unsuccessful introduction of Pt into the compound beyond La_2NiPtO_6 (x = 0.50).

4.2 Structural details for $LaNi_{1-x}Pt_xO_3$ ($0.20 \leq x \leq 0.50$)

The $P2_1/n$ space group and structure of La_2NiPtO_6 includes *B*-site ordering [4], while a *B*-site disordered perovskite is better described in the *Pnma* space group. For the higher symmetry perovskite $LaNiO_3$ (*R-3c*), *B*-site ordering is not allowed by symmetry. In the space group $P2_1/n$, long-range *B*-site ordering is indicated by the intensity of a low angle peak at $Q \approx 1.37$ Å^{-1} [11]. Due to the large difference in atomic number between Ni and Pt, we can expect strong intensity of the peak if the *B*-site is ordered. The peak consists of the (101), (10–1) and (011) Bragg reflections, which all relate to layers with alternating stacking of the two different *B*-site cations (Figure S3). The peak is also allowed in the *Pnma* space group [as (011)], but it always show minimal intensity for disordered perovskites. In this way, the peak is a fingerprint of the long-range ordering of *B*-site cations in perovskites, similar to the descriptions by Meneghini *et al.* [11] on the *B*-site ordering in Sr_2FeMoO_6.

Rietveld refinements of synchrotron XRD data of La_2NiPtO_6 give a good fit using the reported structure model [4] with space group $P2_1/n$ (Figure S1). The cell parameters and volume are very close to the reported values [4]. Refinements of the degree of *B*-site ordering show almost complete *B*-site ordering for La_2NiPtO_6 (Table S3). Ni and Pt are further expected to adopt the oxidation states +II and +IV, respectively, as reported in the literature [2, 4]. This is reasonable considering that the structure is ordered, and in compliance with the empiric rule that *B*-site ordering will only occur if the *B*-elements obtain different oxidation states [14]. Additionally, our magnetic measurements support this conclusion, see below.

Among the monoclinic non-equimolar compositions ($0.20 \leq x \leq 0.40$), the refinements are performed using the same monoclinic structure as La_2NiPtO_6 ($P2_1/n$), however, with replacing an amount of Pt with Ni, as in the substitutional system $La_2Ni_{2-2x}Pt_{2x}O_6$ ($0.20 \leq x \leq 0.50$). For all the monoclinic samples ($0.20 \leq x \leq 0.50$), the analysis provides clear indications of *B*-site ordering (Figure S1), indicated by the intensity of the low angle peak at $Q \approx 1.37$ Å^{-1} (Figure 2). In the $LaNi_{1-x}Pt_xO_3$ sample with $x = 0.05$, the low angle peak at $Q \approx 1.37$ Å^{-1} is absent, but the presence of *B*-site ordering could still be visible through peak broadening or peak splitting. This would be the case if an improved Rietveld refinement fit is obtained with space group $P2_1/n$ compared to *R-3c*. We find that introducing 5 % Pt into $LaNiO_3$ slightly changes the intensities of some of the peaks, but no peak broadening is observed, and the refinements provide similar R_{wp} value for both space group *R-3c* and $P2_1/n$. We therefore conclude that $x = 0.05$ is best described in *R-3c* with the absence of *B*-site ordering.

Upon comparing the synchrotron XRD data of the monoclinic samples ($0.20 \leq x \leq 0.50$; Figure 2), several trends can be seen with increasing the Pt-content. (1) The ordering-peaks ($Q \approx 1.37$ and 2.64 Å^{-1}) intensity increases, (2) all peaks shift towards lower *Q*, *i.e.* larger interatomic distances, (3) the main perovskite peak ($Q \approx 2.26$ Å^{-1}) has a much larger shift towards lower *Q* compared to the ordering-peaks, and (4) the peak shape for the main perovskite peak changes significantly. Furthermore, in the Rietveld refinements of the monoclinic samples ($0.20 \leq x \leq 0.50$), the peaks which indicate *B*-site ordering ($Q \approx 1.37$ Å^{-1} and $Q \approx 2.64$ Å^{-1}), are not well fitted by the structural model. The two peaks are located at a lower *Q* than the average structure

calculated during Rietveld refinements, *i.e.* they correspond to scattering from a region with a larger unit cell volume than the average structure. A different feature is observed for the main perovskite peak, which for a low Pt-content (low x) have an asymmetric tail extending towards higher Q, *i.e.* smaller interatomic distances. In this way, it appears as domains of different size contributes differently to the different peaks; *large unit cell domains* contribute to the *B*-site ordering peaks, while *small unit cell domains* contribute to a tail in the main perovskite peak.

Intuitively, the *large unit cell domains* should contain large Pt-contents and simulate the double perovskite La_2NiPtO_6, and therefore give a strong scattering contribution to the ordering peaks ($Q \approx 1.37$ and 2.64 Å^{-1}). Correspondingly, the *small unit cell domains* may therefore be Ni-rich domains, which contribute to the tail of the main perovskite peak. These factors make it challenging to achieve satisfactory Rietveld refinement fits with a one-structure model. The effect is most prominent for $x = 0.30$, but also strong in $x = 0.20$ and $x = 0.40$, *i.e.* all the monoclinic non-equimolar compositions.

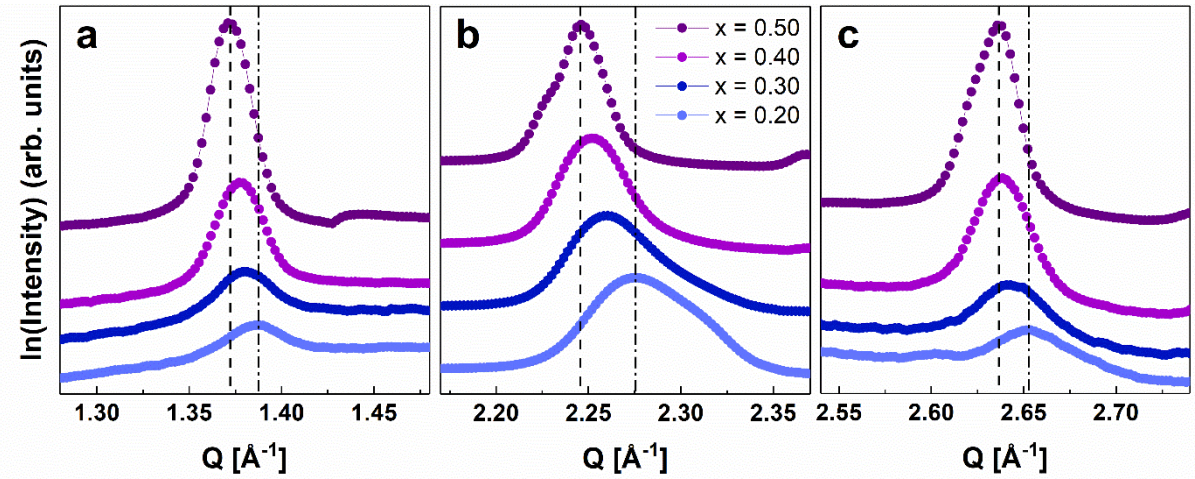

Figure 2. Comparison of low angle peak indicating (a) ordering peak with *hkl* indices (101), (10–1) and (011), (b) main perovskite peak with *hkl* indices (020), (112) and (200) and (c) a higher angle ordering peak with *hkl* indices (121), (013), (211) and (103). The compositions are indicated in the figure. The black dashed and dashed dot lines show the position of the maximum of the peaks for $x = 0.50$ and $x = 0.20$, respectively.

To handle this situation, we expand the structural model for Rietveld refinements into a two-phase (domain) model with one *large* and one *small* unit cell (Table S3), mimicking a composite material with different degrees of Ni/Pt content and ordering. In a first approximation, these two phases (domains) were considered to only differ with respect to unit cell parameters. This significantly improved the fit of the asymmetric peak shape and the fit of the position of the ordering peaks, see Figure 3. Subsequent refinements of the *B*-site occupation indicate that the Pt-content is higher in the *large* cell and lower in the *small* cell, consistent with our expectations (Figure 3c). We also find that the β-angle is larger for the *small* cell and samples with a low Pt-content. The two-phase (domain) model significantly improves the Rietveld refinement fit, which is clearly seen for the main perovskite peak ($Q \approx 2.25$ Å^{-1}) when evaluating the difference curve (Figure 3b). The domain-model is best suited for the samples with $0.20 \leq x \leq 0.40$, while for $x = 0.50$, the single phase model is well suited. Though dependable quantification is difficult to obtain, we believe that the qualitative information gathered is

reliable. The refinements show that Pt has a very strong preference for the Pt-site (2*c*-site), while Ni occupies both *B*-atom sites (2*c* and 2*d* sites) (Table S3). For samples with a lower Pt-content ($x \leq 0.40$), a lower degree of *B*-site ordering is observed, corresponding to the reduced intensity of the peak at $Q \approx 1.37$ Å^{-1}.

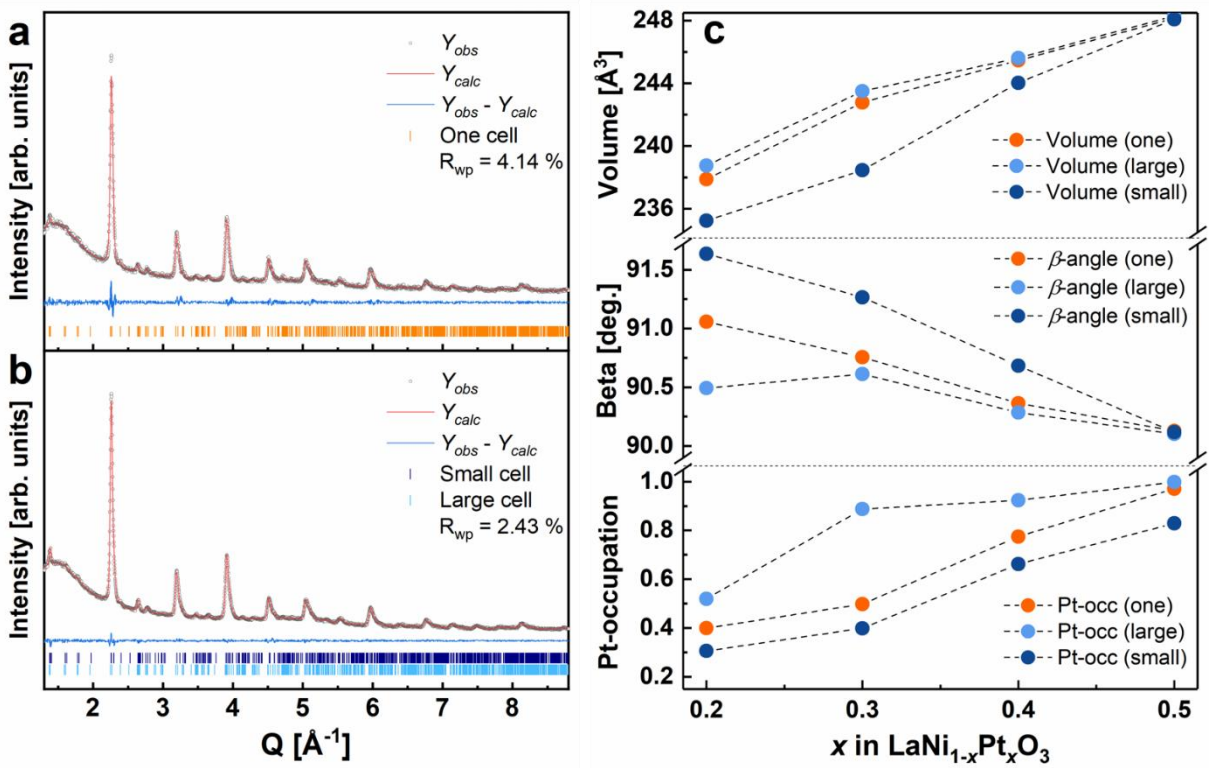

Figure 3: Rietveld refinements of $LaNi_{0.70}Pt_{0.30}O_3$ (*P2₁/n*) using (a) a structure model with a single unit cell and (b) using the two-phase (domain) structure model described in the text, which also refine the *B*-site occupancy of Ni and Pt. The fit of the two-phase (domain) model prove superior to reproduce the experimental diffraction pattern (Table S3). The large bump below 2 Å^{-1} is background from the instrumental setup. (c) Unit cell volume, *β*-angle and Pt-occupation from Rietveld refinements with the one- and two-unit cell model.

We believe the *large* and *small* domains originate from inhomogeneous distribution of Pt. Pt-rich domains contain a more ordered Ni-Pt sub-lattice compared to the average structure, while regions poor in Pt are much less *B*-site ordered. The Pt-rich regions are expected to have larger unit cell parameters and volume in view of the trends shown in Figure 3c. The fact that the samples are synthesized from a wet chemical citric acid-based route indicates a homogenous phase with atomic distribution of the elements during phase formation.

For the DC-magnetization measurements (see below), we performed an extended two weeks long heat treatment in order to obtain less noisy data. By performing this treatment, the XRD pattern for the $x = 0.30$ sample is only slightly changed (Figure S4). The peak width of the main perovskite peak ($Q \approx 2.2$ Å^{-1}) is slightly reduced, but the peak asymmetry, with a tail extending towards higher angles, is still present throughout the diffraction pattern. Though a small difference can be observed in the 1D diffraction pattern (Figure S4), the Debye-Scherrer cones in the 2D-diffraction pattern are smooth, both before and after the two weeks extended heat

treatment (Figure S5). This shows that the sample was homogeneous also before the extended heat treatment, and that the treatment mainly affected macro/microstructural properties. Rietveld refinements after the extended heat treatment (Table S3) show that the domain model still describes the system significantly better than a single-phase model, indicating that the material is still dominated by Pt-rich and Pt-depleted domains. This shows that the described domain-feature is an intrinsic feature of the system, and not a consequence of limited diffusion in the synthesis process. It should be emphasized that the citric acid method was used for synthesis, which ensure good atomic mixing and short diffusion pathways. The Pt-clustering is therefore believed to occur in small nm-sized domains inside grains, similar to the ordering phenomena well described by Meneghini *et al.* for Sr_2FeMoO_6 [11]. In Sr_2FeMoO_6, different degree of long-range ordering of Fe and Mo can be achieved by different synthesis protocols. However, the short-range ordering of Fe and Mo is always present, regardless of long-range order observed by XRD. For $LaNi_{1-x}Pt_xO_3$, we may have a very similar situation. The main differences are that (1) Pt has a very high preference for the Pt-site (2*c*-site) in the structure, and (2) we are additionally considering disorder in non-equimolar compounds.

Based on the current findings, we can now prepare a model of the microstructure of $LaNi_{1-x}Pt_xO_3$ in the ionic approximation. For La_2NiPtO_6, a Ni atom located next to a Pt(IV)-octahedra will adopt a +II oxidation state, and the oxygen in between them –II. When a Pt(IV) atom is replaced by a Ni atom, this Ni atom will adopt an oxidation state of +III. To keep charge neutrality, another Ni(III) must also be generated by oxidation of another Ni(II) to Ni(III). Thus, we find it more appropriate to describe the system by the formula $La_2Ni^{II}_yNi^{III}_{2-2y}Pt^{IV}_yO_6$, $0 \leq y \leq 1$, with end members $LaNi^{III}O_3$ ($y = 0$) and $La_2Ni^{II}Pt^{IV}O_6$ ($y = 1$). Consequently, Ni(III)-O-Ni(II) segments are present in the structure for the non-equimolar compositions ($0.20 \leq x \leq 0.40$), and the oxygen atom located between them will be uncompensated in terms of charge. Therefore, there are three different oxygen atoms depending on which elements they are positioned between; Ni(III)-O-Ni(III), Ni(II)-O-Pt(IV) or Ni(II)-O-Ni(III), see Figure 4a. The Ni(II)-O-Ni(III) segment deviate from the ionic approximation and the oxygen atoms of these segments will interact with its nearby Ni-atoms to find the most appropriate charge distribution.

To minimize the energy of the system, the number of uncompensated oxygen atoms must be reduced as much as possible. By evaluating both a clustering of Pt atoms (Figure 4b) and random distribution (Figure 4c), we observe that the number of uncompensated oxygen atoms can be reduced by forming clusters. The Pt rich clusters can in this way form boundaries of uncompensated oxygen atoms, which supports the observed phase separation in the system, simply by an energy minimization. The energy gain for clustering must therefore be significant. On the other hand, if the energy gain was substantial, we would have expected a wider immiscibility gap, with low solubility of Pt into $LaNiO_3$ and of Ni into La_2NiPtO_6. However, the observed two-phase region is narrow ($0.075 \leq x \leq 0.125$), indicating that the driving force for clustering is strong at a local scale, but not as strong on a long-range scale. The origin behind the phenomena of local ordering and clustering of Pt-rich regions remains to be explained, and local probes such as transmission electron microscopy (TEM), total scattering analysis (PDF) and X-ray absorption spectroscopy (XAS), along with other average structure techniques such as neutron diffraction (ND), may be needed to understand it.

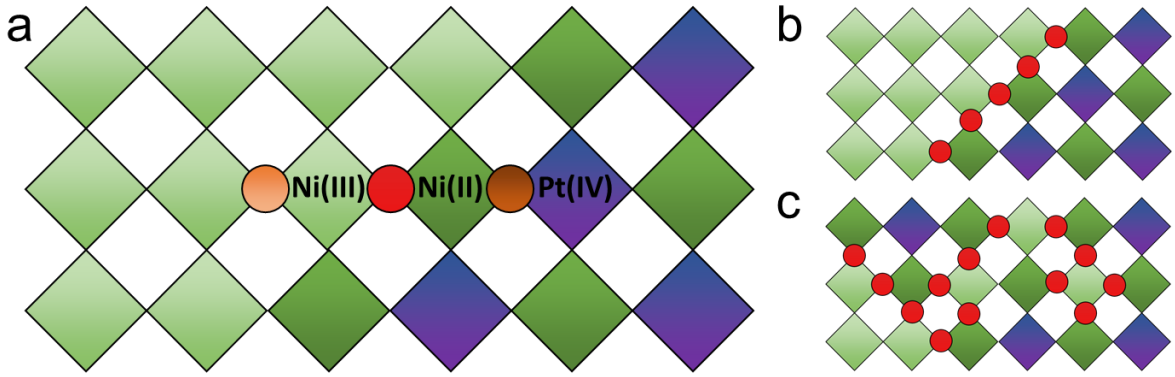

Figure 4. (a) Illustration of the different "type" of octahedral corner sharing oxygen ions (the circles) in $LaNi_{1-x}Pt_xO_3$. The bright orange oxygen ions are positioned between two Ni(III) ions, the red is positioned between one Ni(II) and one Ni(III) ion, and the brown in positioned between one Ni(II) and one Pt(IV) ion. (b) Illustration of the number of uncompensated O-ions in the case of clustering and (c) random Pt-distribution.

4.3 Magnetic properties

4.3.1 Paramagnetic region ($T > 100$ K)

$LaNiO_3$ is found to be Pauli paramagnetic in the temperature interval 4-300 K (Figure S6), in compliance with earlier reports on $LaNiO_3$ powders [19]. Upon substituting Pt into $LaNiO_3$, as in $LaNi_{1-x}Pt_xO_3$, the Pauli paramagnetic behaviour changes to regular temperature dependent paramagnetism for $x = 0.05$, as well for all other samples (Figure 5 and Figure S7). At elevated temperature (~100-300 K), these samples follow a linear Curie-Weiss relationship (Figure S8). For the $x = 0.20$, 0.30 and 0.40 samples prepared, after following only the initial synthesis protocol (2×12 hours' heat treatment), the Curie-Weiss region deviated slightly from linear behaviour. After extended heat treatments (two additional weeks), the susceptibility is slightly lowered, and the Curie-Weiss region is more pronounced (Figure S9). We suggest that macro/microstructural changes caused by the heat treatment is the origin of this effect, as the structural domain model still describes the system best also after the extended heat treatment (see above).

Curie-Weiss analysis further yields a highly negative θ-value for all analysed compositions, and a paramagnetic moment in the range of 2.4 – 3.1 μ_B, see Table 1. The paramagnetic moment is approximately unchanged through the compositional series, *i.e.* it is almost invariant with respect to the Pt-content. Based on the proposed chemical formula from the ionic approximation (see above), $La_2Ni^{II}_yNi^{III}_{2-2y}Pt^{IV}_yO_6$, and assuming Ni(III) is in the low spin state, the electronic configuration at the *B*-site for $0 \leq y \leq 1$ ($0 \leq x \leq 0.50$) will be:

$$yNi^{II} + (2-2y)Ni^{III} + yPt^{IV} \rightarrow y\left(t_{2g}^6 e_g^2\right) + (2-2y)\left(t_{2g}^6 e_g^1\right) + y\left(t_{2g}^6 e_g^0\right)$$

We see that the average number of unpaired electrons at the *B*-site will always be one. In the spin-only approximation [20], this results in a minimal change in the paramagnetic moment

through the compositional series (Table 1), and comply well with our observation of a similar paramagnetic magnetic moment for all compositions.

Notably, all compositions show a slightly higher magnetic moment than the spin-only approximation, especially x = 0.05, 0.25 and 0.50 (Table 1). The elevated magnetic moment may have several origins, such as small amounts of magnetic impurities, an unexpected high-spin state of Ni(III), spin orbit coupling, or microstructural effects (surfaces-/interfaces). Firstly, magnetic impurities are unlikely. The only impurity observed with XRD is Pt-metal for x = 0.50, which does not contribute to the Curie-Weiss paramagnetic moment as Pt is a Pauli paramagnetic metal. The spin state of Ni or spin orbit coupling could in combination explain the elevated magnetic moment, but our experimental data cannot confirm either scenario.

With respect to structural effects, both the degree of *B*-site ordering [12] and the existence of surface states [21] are known to affect magnetic properties. In $LaNi_{1-x}Pt_xO_3$, the local Ni-Pt ordering inside domains, and the interface between domains, may therefore induce magnetic phenomena not possible to describe by this simple approximation. We have clearly seen the effect of extended heat treatments on the magnetic susceptibility (Table 1 and Figure S9), and believe the sample homogeneity and macro/microstructure is related to the observed magnetic moment. We therefore conclude that the spin-only approximation describes well the paramagnetic moments of these samples, and that the microstructure contributes with minor additional effects.

Table 1. Experimental magnetic moment and the θ-value calculated using the Curie-Weiss relation, and the theoretical magnetic moment calculated from the spin-only approximation [20].

x	0.05	0.20*	0.20**	0.25	0.30	0.40	0.50
m(exp.)	2.7	2.7	2.4	3.1	2.6	2.4	2.9
m(theory)	1.76	1.84	1.84	1.87	1.90	1.95	2.00
θ $[K]$	−1027	−350	−322	−354	−194	−111	−130

*Standard heat treatment procedure, **Sample heated for two additional weeks.

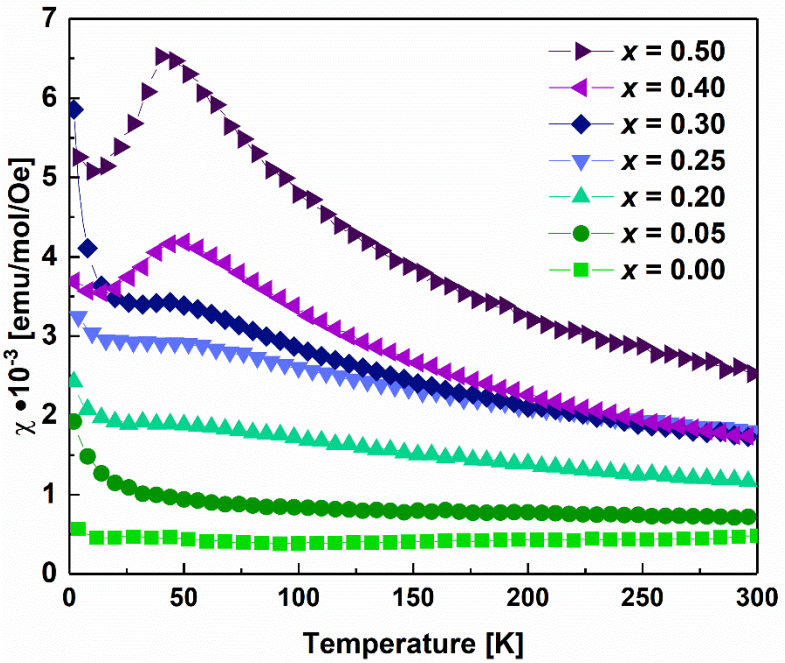

Figure 5. Zero field cooled (ZFC) DC magnetization measurements of $LaNi_{1-x}Pt_xO_3$ ($0 \leq x \leq 0.50$) using a 2000 Oe external DC-field. The sample compositions are indicated in the figure.

4.3.2 Antiferromagnetic transition at low temperature

For La_2NiPtO_6, the DC magnetic susceptibility show a clear drop below ~40 K, consistent with long-range antiferromagnetic ordering (Figure 5). The transition also occurs for all monoclinic samples ($x \geq 0.20$), *i.e.* with *B*-site ordering, but not for $x = 0.05$. However, the transition gets much less pronounced with reducing Pt-content, and for $x \leq 0.30$ the transition is visible only as a small step in the susceptibility. This is probably due to a significant paramagnetic contribution upon further cooling, resulting from the fact that the non-equimolar samples contain less of the long-range Ni-Pt structural ordering. Still, the transition temperature (T_N) is seemingly unaffected and changes very little with Pt-content (Figure 5). The fact that $x = 0.05$ is structurally described by *R-3c* indicates that this sample could still be metallic [22], and it may not be dominated by the same mechanisms as the other samples.

To understand the low temperature magnetic properties of this system, field dependent DC magnetic measurements were performed at 4 K, see Figure 6a. The magnetization is low for all samples, and the lowest magnetization is observed for samples with low x (low Pt-content). It is therefore likely that an AFM ground state dominates all samples, with some differences depending on the Ni/Pt content. This correlates well with the negative theta value from the Curie-Weiss analysis (Table 1), which showed increasingly negative values for samples with a low x (low Pt-content). Additionally, the field dependent magnetization measurements show an upswing at high magnetic fields for several of the compositions, most prominent for $x = 0.40$ and $x = 0.50$ (Figure 6a). This is evident from the derivative of the magnetization (Figure 6b), which for these samples increases for fields above 1 T. The phenomenon is quite weak, show no signs of saturation up to 9 T, and its origin is unknown. It could simply come from the fact that we transition from a strong ($x = 0.05$; short range interactions) to weak ($x = 0.50$; long

range ordered) antiferromagnet with increasing Pt-substitution, causing the Pt-rich samples to be more affected by the external field. Additionally, if there is a small degree of disorder, *e.g.* a few percent mixing in Ni-Pt ordering, structural strain, inter-grain effects, or magnetostriction, this could cause different canting of the spins in the magnetic field, resulting in variating effects in the field dependent magnetization. We find it unlikely that this effect is coming from changes in magnetic interactions or electron configuration.

To further investigate the AFM transition at ~40 K, AC magnetic measurements was performed for two compositions, x = 0.25 and x = 0.50, see Figure 7. For La_2NiPtO_6, χ' show similar behaviour as the DC magnetization; there is a drop in the susceptibility below ~42 K and the AFM transition show no frequency dependence. χ'' is generally noisy and close to zero, but a weak peak is observed above the transition temperature. This indicates that the AFM transition may start at a higher temperature than indicated from χ'. However, we still believe that La_2NiPtO_6 is near being a pure antiferromagnet. For x = 0.25, χ' show an increase in susceptibility below T_N (Figure 7), while χ'' is noisy and close to zero. The behaviour contrasts that of La_2NiPtO_6, especially the different behaviour of χ' (Figure 7), indicating a deviation from pure antiferromagnetism for x = 0.25. In this way, all the non-equimolar compositions may be different compared to the equimolar La_2NiPtO_6 (x = 0.50).

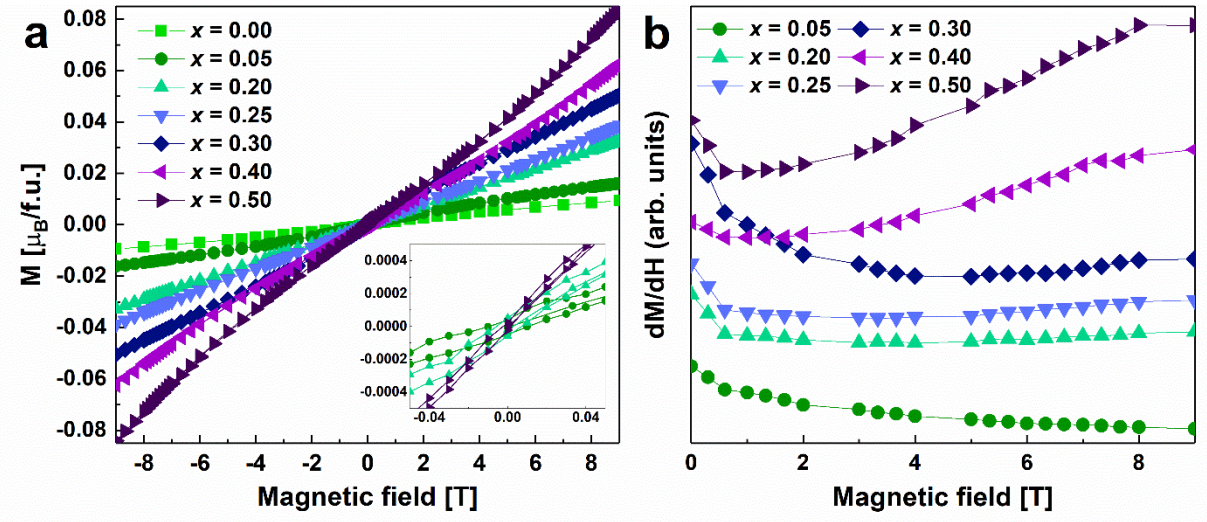

Figure 6. (a) Field dependent DC magnetic measurements from –9 to 9 T at 4 K, and (b) the derivative of the magnetization (x = 0.00 is included in Figure S10). The formula unit (f.u.) used is $LaNi_{1-x}Pt_xO_3$ for all samples. The increase in derivative towards H = 0 T is due to a slight non-linearity near H = 0 T.

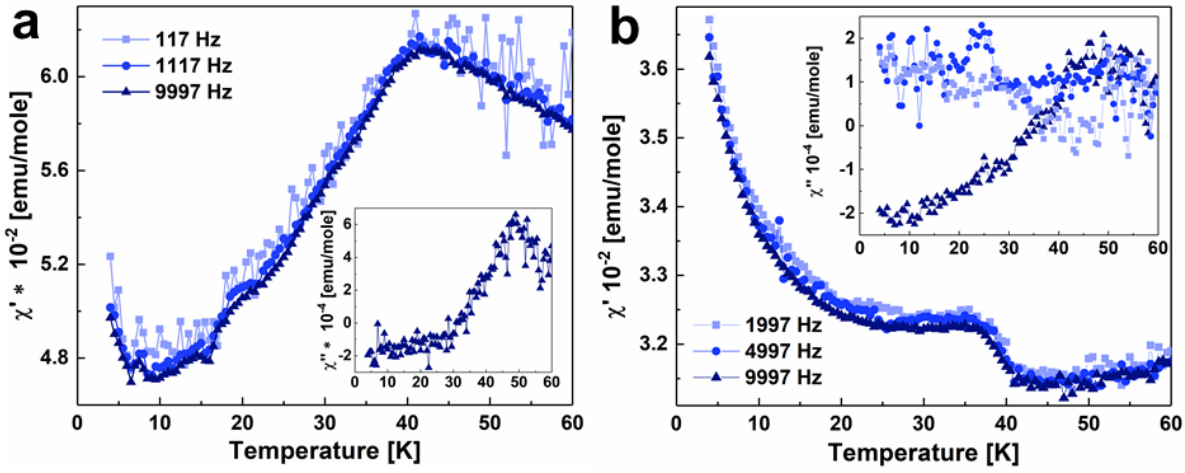

Figure 7. AC magnetization measurements of a) La_2NiPtO_6 using a 10 Oe AC field, and b) of $LaNi_{0.75}Pt_{0.25}O_3$ using a 15 Oe AC field. The real component of the susceptibility (χ') is shown in the main figure, and the imaginary component of the susceptibility (χ'') is shown in the inset.

5. Discussion

We have shown how Pt-substitution causes disorder in the non-equimolar compositions in $LaNi_{1-x}Pt_xO_3$ ($0.20 \leq x \leq 0.40$), and that a domain-structure appears with Pt-rich domains, with large degree of *B*-site ordering, and Pt-depleted domains, with low degree of *B*-site ordering. The present investigation draws similarities to the structural disorder in Sr_2FeMoO_6 [11]. Locally, Ni-Pt ordering is favoured in a similar way as Fe-Mo ordering is favoured, a property that has strong influence on the magnetic interactions in the systems. As presented above, the most evident antiferromagnetism exists in La_2NiPtO_6, which becomes less pronounced for samples with lower Pt content. The samples with less Pt ($x \leqslant 0.40$) consist of local domains of high Pt-content and *B*-site ordering, which are probably dominated by the same AFM interactions as La_2NiPtO_6. The magnetization decreases from high ($x = 0.50$) to low ($x = 0.05$) Pt-content in the field dependent magnetization (Figure 6), indicating a reduced ability of the Pt-depleted samples to become magnetized. As the AFM transition becomes less evident with lower Pt-content (Figure 5), we suggest that the Pt-depleted domains remain in a paramagnetic state, but with short-range AFM interactions. The susceptibility for $0.20 \leqslant x \leqslant 0.40$ can thus be considered as a combination of the paramagnetic $x = 0.05$ and antiferromagnetic $x = 0.50$ samples (Figure S11), as if the antiferromagnetic ordering of $x = 0.50$ is simply diluted by the Pt-depleted domains. This indicates that the magnetic interactions are unchanged through the system; there is only a change in the quantity depending on the Pt-content in the samples. If the system showed a trend with changing oxidation states, such as in $LaNi_{1-x}Rh_xO_3$ [23], a change in magnetic interaction mechanism should have occurred. The results therefore correlate well with the structural domain model, showing that ordered antiferromagnetic domains (Pt-rich domains) coexist with paramagnetic domains (Pt-depleted domains) for $0.20 \leqslant x \leqslant 0.40$, where the latter is dominated by short-range AFM interactions.

Regarding the magnetic interactions in La_2NiPtO_6, there are several similarities between the two stoichiometric double perovskites La_2NiPtO_6 and La_2NiTiO_6 [24]; both are weakly antiferromagnetic at low temperature, and the second *B*-site elements have very similar electronic configurations: $t_{2g}^0 e_g^0$ for Ti(IV) and $t_{2g}^6 e_g^0$ for Pt(IV). We speculate if the full t_{2g}-orbitals of Pt(IV) are participating or not with respect to magnetic interactions in La_2NiPtO_6. If there is no interaction of the full t_{2g}-orbitals of Pt, the two compounds should be dominated by similar magnetic interactions, namely the super-super exchange interaction between the e_g- and *p*-orbitals through Ni-O-(Ti/Pt)-O-Ni, as in La_2NiTiO_6 [24]. However, in La_2CoPtO_6 [2] a hybridization mechanism is suggested for the interaction between Co(II) high-spin ($t_{2g}^5 e_g^2$) and the full t_{2g}-orbital of Pt(IV) [2]. Here, the t_{2g}-orbital of Co(II) is only partially filled, allowing the unpaired t_{2g}-electron of Co(II) to hybridize with the Pt(IV) t_{2g}-orbital. Because the Pt(IV) t_{2g}-orbital is full, both FM and AFM coupling with Co(II) is possible, resulting in a weak magnetic interaction and low ordering temperature [2]. This shows that even though the t_{2g}-orbital of Pt(IV) is full, it can participate in magnetic interactions when the neighbouring element have unpaired t_{2g}-electrons. Unlike La_2CoPtO_6, in the scenario with Ni(II)($t_{2g}^6 e_g^2$)/Ti(IV)($t_{2g}^0 e_g^0$) and Ni(II)($t_{2g}^6 e_g^2$)/Pt(IV)($t_{2g}^6 e_g^0$), both *B*-site elements have full/empty t_{2g}-orbitals, and the t_{2g}-orbitals are much less likely to participate in magnetic interactions. It is therefore plausible that the magnetic interactions dominating La_2NiPtO_6 are more similar to that of La_2NiTiO_6, with mainly super-super exchange interactions through the e_g-*p*-orbitals, resulting in an AFM ground state for both compounds.

Assuming that the super-super exchange interaction above is the dominating magnetic interaction in La_2NiPtO_6, it should also dominate the Pt-rich domains with large degree of *B*-site ordering in $LaNi_{1-x}Pt_xO_3$ ($0.20 \leq x \leq 0.40$). With respect to the Pt-depleted domains dominated by strong short-range AFM interactions, Ni(III) is the dominating species, which is heavily investigated in both metallic and insulating nickelates [22, 25, 26]. At low temperatures, the insulating $YNiO_3$ is reported to be antiferromagnetic with a charge disproportionation of Ni(III) to Ni(III + δ) and Ni(III – δ), resulting in a monoclinic structure and two different Ni-sites [25]. Charge disproportionation of Ni(III) is also relevant for our compounds, as it shows how Ni(III) is intrinsically unstable in an insulating oxide matrix. Upon Pt-substitution in $LaNi_{1-x}Pt_xO_3$, the same charge disproportionation of Ni(III) may occur once the compound turns insulating. One can imagine that Ni-atoms located at the Pt-site (2*c*-site) will exist as Ni(III + δ). Correspondingly, Ni(III – δ) must be present at the Ni-site (2*d*-site). Such an electronic disproportionation is not limited to insulating nickelates, but is also reported for metallic nickelates, as shown by Li *et al.* [27], who described insulating pockets in $LaNiO_3$ using PDF. In order to understand these systems, one certainly needs to look well beyond any ionic approximation. Local structure investigations (TEM, PDF, XAS) may be a necessity to understand how the electronic landscape is changed by introducing dopants, and how that affects both insulating and metallic nickelates.

6. Conclusions

We have demonstrated that the system $LaNi_{1-x}Pt_xO_3$ ($0 \leq x \leq 0.50$) undergoes a change in oxidation states upon Pt-substitution, causing the system to be better described by the formula

$La_2Ni_y^{II}Ni_{2-2y}^{III}Pt_y^{IV}O_6$, $0 \leq y \leq 1$. Because Pt has a strong preference for the Pt-site (2*c*-site) in the monoclinic structure of La_2NiPtO_6 (*P2₁/n*), and adopts only the +IV oxidation state, it becomes unfavourable to randomly distribute Pt at the *B*-site for the non-equimolar compositions in $LaNi_{1-x}Pt_xO_3$ ($0.20 \leq x \leq 0.50$) due to issues of charge balance on the nearby Ni- and O-atoms. Although a wet-chemical synthesis route is used, clustering of Pt-rich and Pt-depleted domains occurs inside the sample, also after an additional two weeks long heat treatment, demonstrating that the domain structure is an energetically favourable state. Only the Pt-rich samples with a large degree of structural long-range order show a distinct antiferromagnetic transition at low temperature ($T_N \approx 40$ K). For $0.20 \leqslant x \leqslant 0.40$, the magnetization decreases from high to low Pt-content simultaneously as the Néel-point (~40 K) becomes less pronounced, as if the antiferromagnetism of $x = 0.50$ is diluted by paramagnetic Pt-depleted domains with short-range AFM interactions. The electronic configuration of this system draws clear similarities to that of La_2NiTiO_6, indicating that both systems may be dominated by the same antiferromagnetic interaction (super-super-exchange). This would explain why the Pt-rich samples show the most distinct Néel-point.

7. Acknowledgements

The authors would like to acknowledge the help of Dr. Susmit Kumar with magnetic measurements and discussions on this topic, along with Associate Professor Björn Martin Valldor. We also acknowledge the expertise of the Swiss-Norwegian Beam Lines at ESRF, Grenoble. In addition, we greatly appreciate discussions on structure-property relations in the NAFUMA group at the University of Oslo. The project was financed by the Research Council of Norway through the projects RIDSEM (project no. 272253) and iCSI (project no. 237922).

8. Supplementary information

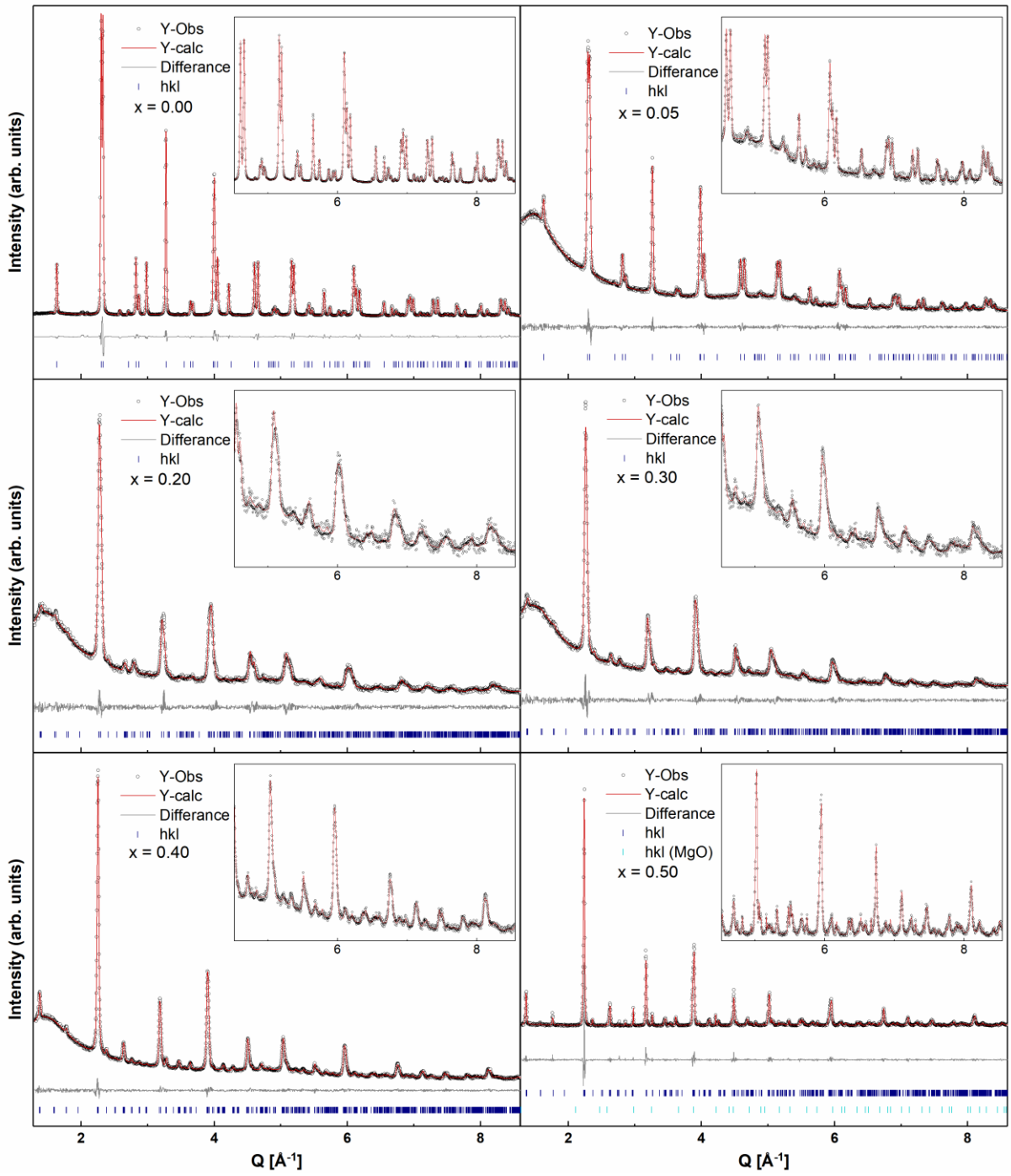

Figure S1. Rietveld refinement of $LaNi_{1-x}Pt_xO_3$ using the single phase model and space group *R-3c* for x = 0.00 and x = 0.05 and *P2₁/n* for $x \geq 0.20$; λ = 0.50506 Å for x = 0.00 and x =0.50 and λ = 0.50467 Å for x = 0.05, 0.20, 0.30 and 0.40. Dark blue tics represent Bragg reflections from $LaNi_{1-x}Pt_xO_3$ (*R-3c* or *P2₁/n*), and cyan tics represent Bragg reflections from MgO (*Fm-3m*), which was used to reduce absorption for La_2NiPtO_6.

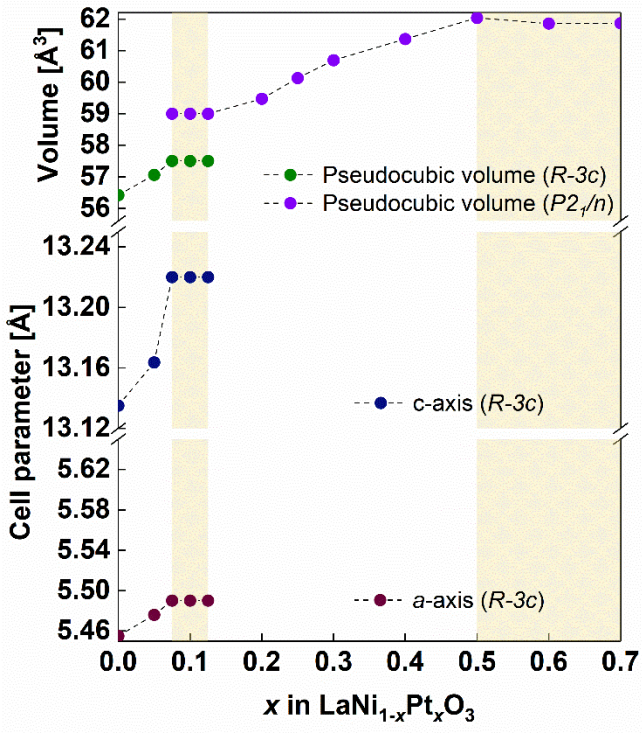

Figure S2. Cell parameters for the rhombohedral samples in $LaNi_{1-x}Pt_xO_3$, along with the pseudocubic volume.

Table S1. Crystallographic information for $LaNi_{0.95}Pt_{0.05}O_3$ obtained from Rietveld refinements of XRD data with a one-unit cell model, with $a = b = 5.476$ Å, $c = 13.164$ Å and $\gamma = 120°$ in *R-3c*.

Site	Atom	Wyckoff	*x*	*y*	*z*	Occ	B_{iso}
La1	La+3	6a	0	0	0.25	1	1.170(13)
Ni1_1	Ni+3	6b	0	0	0	0.9	0.420(17)
Ni1_2	Ni+2	6b	0	0	0	0.05	0.420(17)
Ni1_3	Pt+4	6b	0	0	0	0.05	0.420(17)
O1	O-2	18e	0.4601(15)	0	0.25	1	2.90(17)

Table S2. Crystallographic information for La_2NiPtO_6 obtained from Rietveld refinements of XRD data with a one-unit cell model, with $a = 5.578$ Å, $b = 5.629$ Å, $c = 7.903$ Å and $\beta = 90.13°$ in $P2_1/n$.

Site	Atom	Wyckoff	*x*	*y*	*z*	Occ	B_{iso}
La1	La3+	4e	0.5027(6)	0.5449(2)	0.2498(3)	1	0.76(3)
Ni1_1	Ni2+	2d	0.5	0	0	0.972(3)	0.41(6)
Ni1_2	Ni3+	2d	0.5	0	0	0	0.41(6)
Ni1_3	Pt4+	2d	0.5	0	0	0.028(3)	0.41(6)
Pt1_1	Pt4+	2c	0	0.5	0	0.972(3)	0.464(18)
Pt1_2	Ni3+	2c	0	0.5	0	0.028(3)	0.464(18)
O1	O2-	4e	0.223(4)	0.219(4)	0.950(4)	1	0.4(2)
O2	O2-	4e	0.285(4)	0.696(4)	0.961(4)	1	0.4(2)
O3	O2-	4e	0.401(6)	0.999(3)	0.246(3)	1	0.4(2)

Table S3. Results from structural analysis and Rietveld refinements of selected members in the $LaNi_{1-x}Pt_xO_3$ series. The Pt-occupancy is the occupancy of Pt on the 2*c*-site in $P2_1/n$ and 6*b*-site in *R-3c*, while the rest of the *B*-atom are occupied by Ni (Ni-site in $P2_1/n$ is 2*d*-site). For $x = 0.50$, the two structures in the domain

model have very similar dimensions. This shows that the model is best suited only for the non-equimolar compositions. Due to broad peaks, the crystallite sizes are calculated without subtracting the instrumental peak broadening. Additionally, as the peak broadening may originate from sub-particle domains, the calculated crystallite size is mainly appropriate to describe the domain size, not the particle size.

x, domain model	Unit cell size	Phase fraction	a [Å]	b [Å]	c [Å]	beta [°]	Volume [Å^3]	Rwp	Cry. Size [nm]	Pt-occ (theory)	Pt-occ (exp)
0.05	"large"	56 %	5.482		13.183		343.1		18	0.05	0.03
0.05	"small"	44 %	5.469		13.145		340.5	2.4	25	0.05	0.07
0.20	"large"	44 %	5.572	5.535	7.742	90.5	238.7		15	0.40	0.52
0.20	"small"	56 %	5.519	5.500	7.753	91.6	235.2	3.1	12	0.40	0.31
0.30 (regular)	"large"	41 %	5.581	5.580	7.821	90.6	243.5		18	0.60	0.89
0.30 (regular)	"small"	59 %	5.545	5.556	7.742	91.3	238.5	2.4	10	0.60	0.40
0.30 (annealed)	"large"	55 %	5.573	5.595	7.812	90.6	243.6		22	0.60	0.65
0.30 (annealed)	"small"	45 %	5.571	5.561	7.749	91.6	240.0	7.5	14	0.60	0.55
0.40	"large"	52 %	5.575	5.603	7.863	90.3	245.6		24	0.80	0.92
0.40	"small"	48 %	5.560	5.603	7.835	90.7	244.0	2.7	10	0.80	0.66
0.50	"large"	76 %	5.574	5.636	7.905	90.1	248.3		34	1.00	1.00
0.50	"small"	24 %	5.596	5.615	7.894	90.1	248.1	13.2	57	1.00	0.83
x, simple model	**Unit cell size**	**Phase fraction**	**a [Å]**	**b [Å]**	**c [Å]**	**beta [°]**	**Volume [Å^3]**	**Rwp**	**Cry. Size [nm]**	**Pt-occ (theory)**	**Pt-occ (exp)**
0.05	avg	1	5.476		13.164		341.8	2.9	43	0.05	
0.20	avg	1	5.544	5.537	7.752	91.1	237.9	4.6	22	0.40	0.40
0.30 (regular)	avg	1	5.569	5.584	7.807	90.8	242.8	4.1	37	0.60	0.51
0.30 (annealed)	avg	1	5.579	5.585	7.813	90.7	243.4	9.9	16	0.60	0.60
0.40	avg	1	5.579	5.598	7.860	90.4	245.5	2.8	81	0.80	0.78
0.50	avg	1	5.578	5.629	7.903	90.1	248.1	16.3	155	1.00	0.97

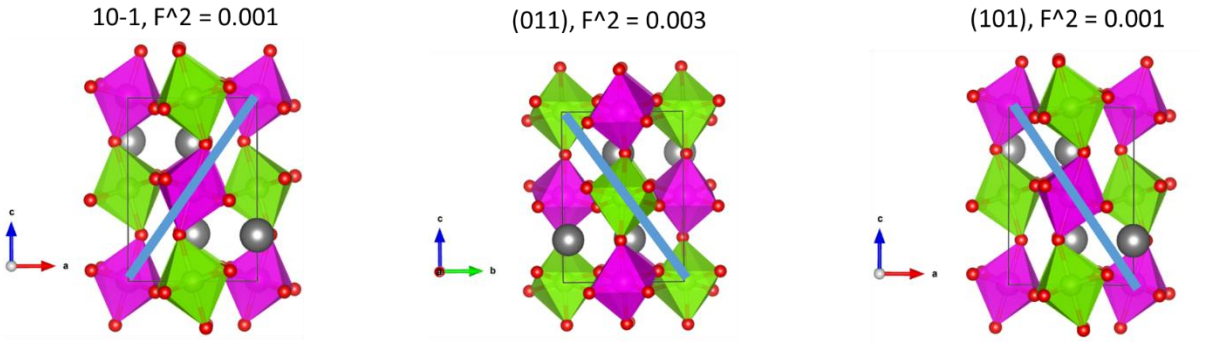

Figure S3. Example of crystallographic planes associated with *B*-site ordering in the double perovskite La_2NiPtO_6 (*P2₁/n*).

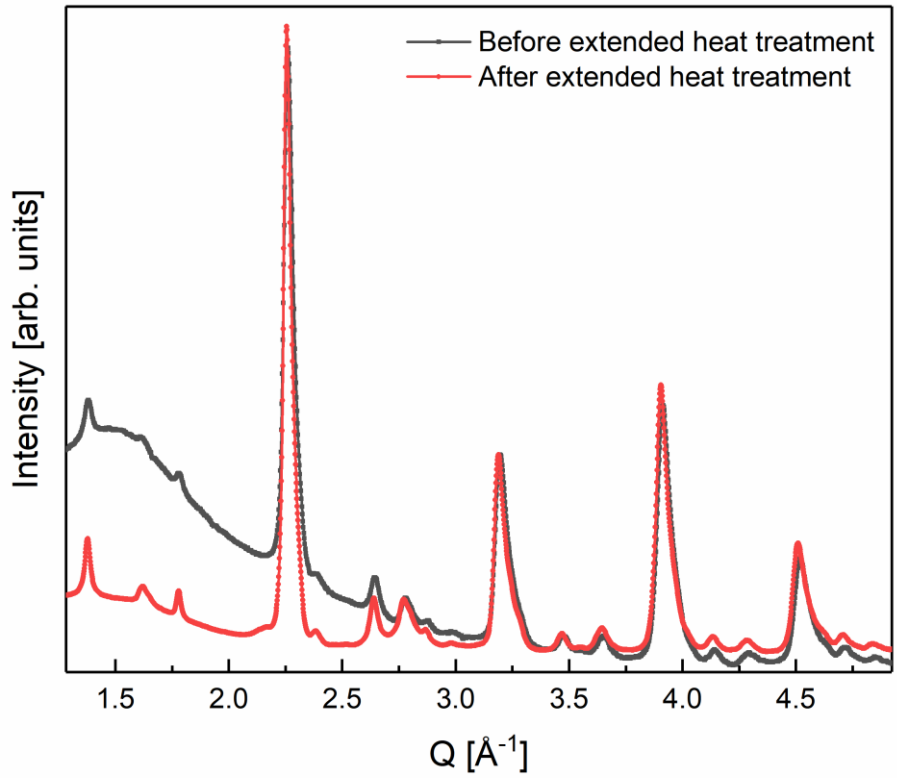

Figure S4. Synchrotron XRD of $LaNi_{0.70}Pt_{0.30}O_3$ before and after the extended two weeks long heat treatment. λ = 0.50467 Å (before heat treatment) and λ = 0.71490 Å (after heat treatment). The difference in background at low scattering angle is from the different experimental setups.

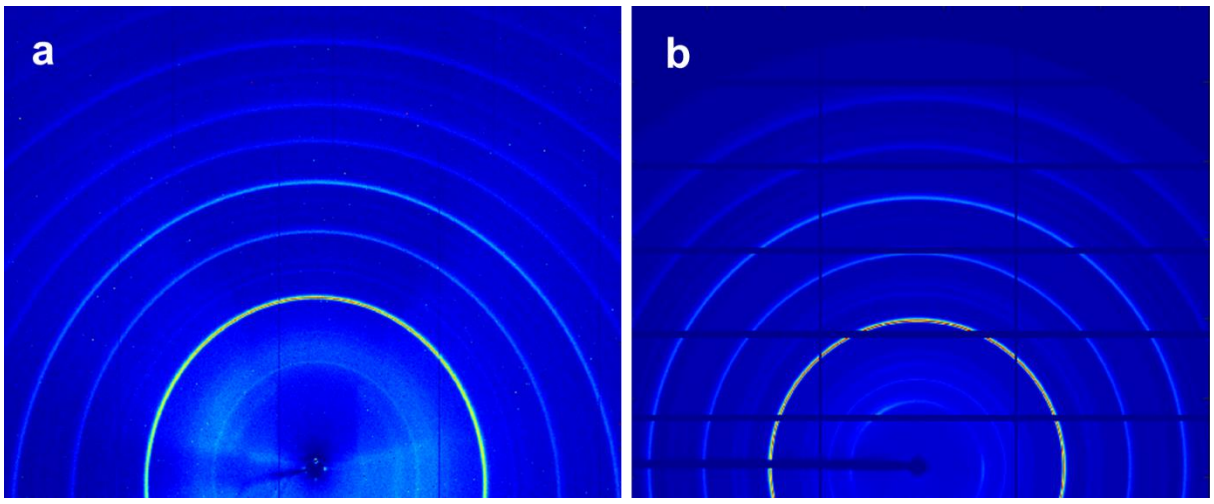

Figure S5. 2D X-ray diffraction pattern from a) a 2D Dexela detector of $LaNi_{0.70}Pt_{0.30}O_3$ before the 2 weeks extended heat treatment (λ = 0.50467 Å) and b) a 2D Pilatus detector of $LaNi_{0.70}Pt_{0.30}O_3$ after the 2 weeks extended heat treatment (λ = 0.71490 Å). The variating intensity in the inner rings is scattering from the sample setup. The pictures are generated using Albula and matlab R2017a.

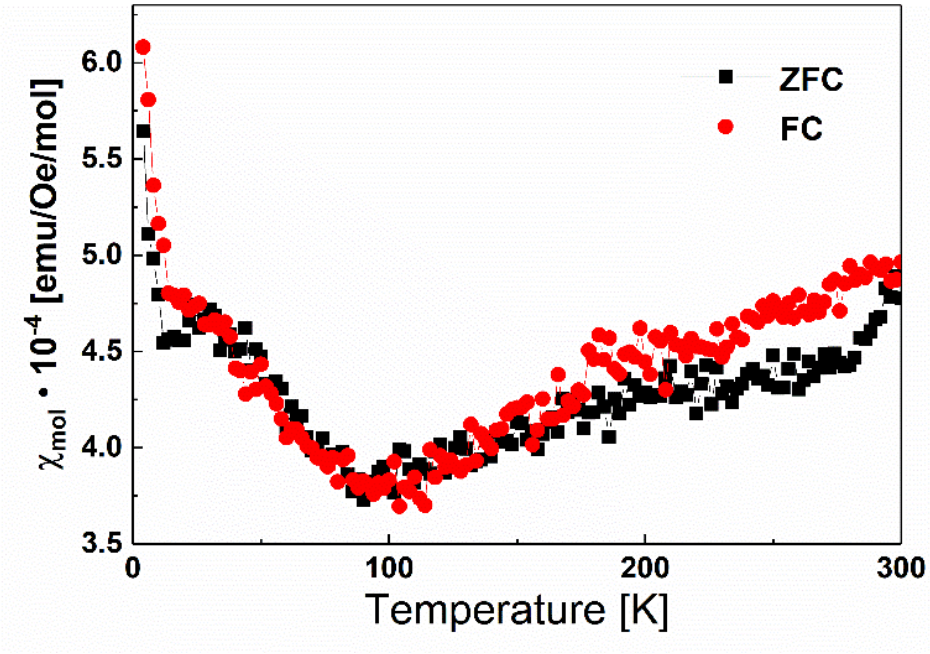

Figure S6. Zero field cooled (ZFC) and field cooled (FC) DC magnetization measurement of $LaNiO_3$ using a 2000 Oe external DC-field.

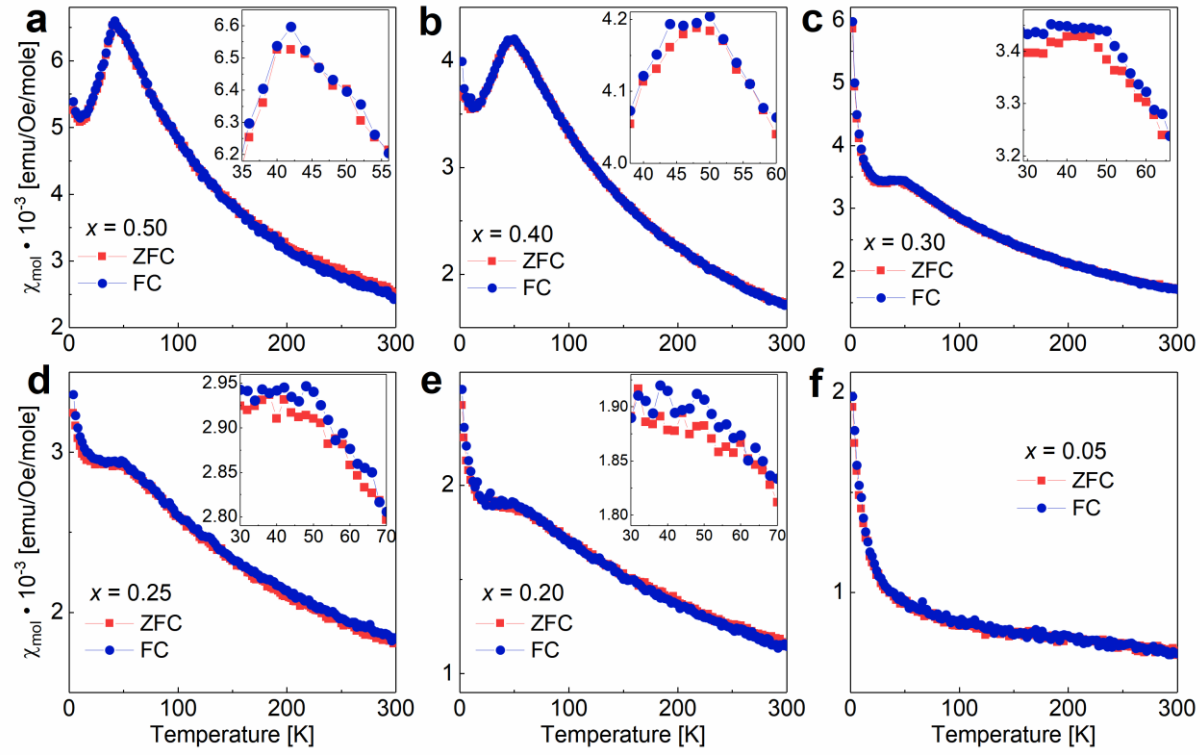

Figure S7. Zero field cooled (ZFC) and field cooled (FC) DC magnetization measurements of $LaNi_{1-x}Pt_xO_3$ ($0.05 \leq x \leq 0.50$) using a 2000 Oe external DC-field. The sample compositions are indicated in the figure.

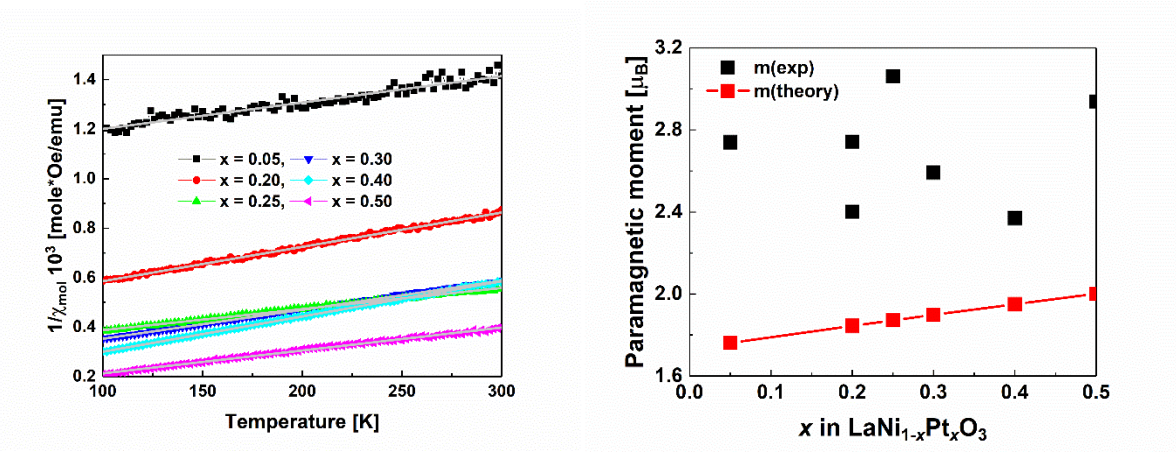

Figure S8. Linear fit of 1/χ using the Curie-Weiss relation (left) and the obtained magnetic moment compared with theoretical magnetic moment (right).

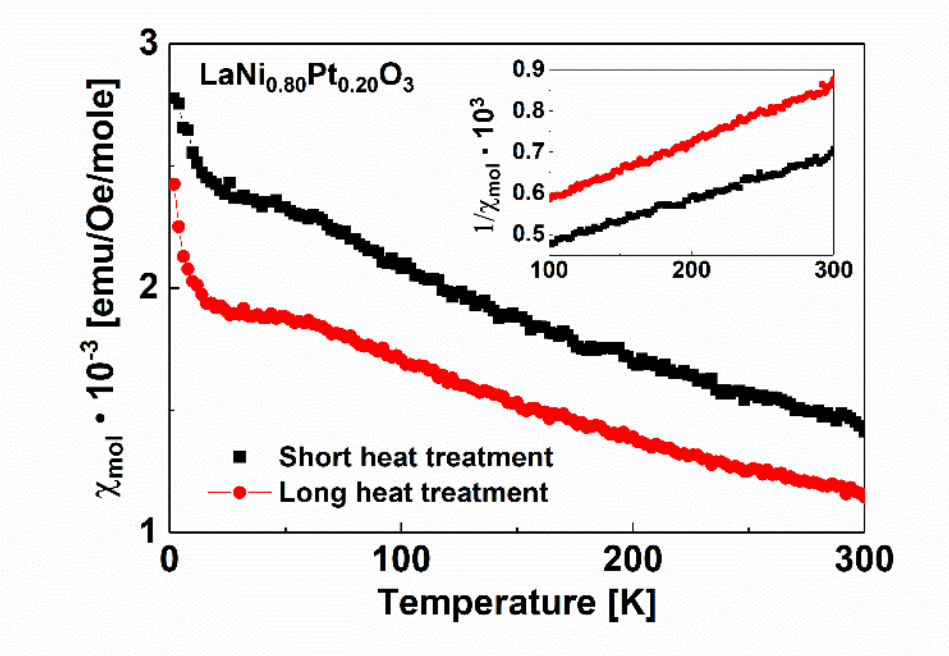

Figure S9. Comparison between ZFC magnetic measurement of $LaNi_{0.80}Pt_{0.20}O_3$ after a short (2×12 hours) and long (additional two weeks) heat treatment. χ_{mol} is shown in the figure and $1/\chi_{mol}$ is shown in the inset.

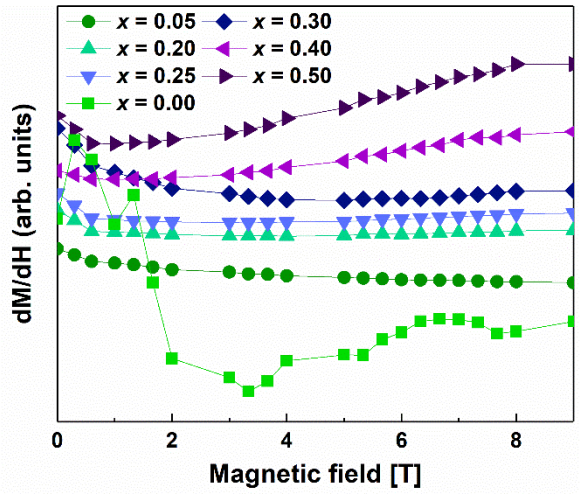

Figure S10. The derivative of the field dependent magnetization 0 to 9 T at 4 K (Figure 6) for all samples in $LaNi_{1-x}Pt_xO_3$.

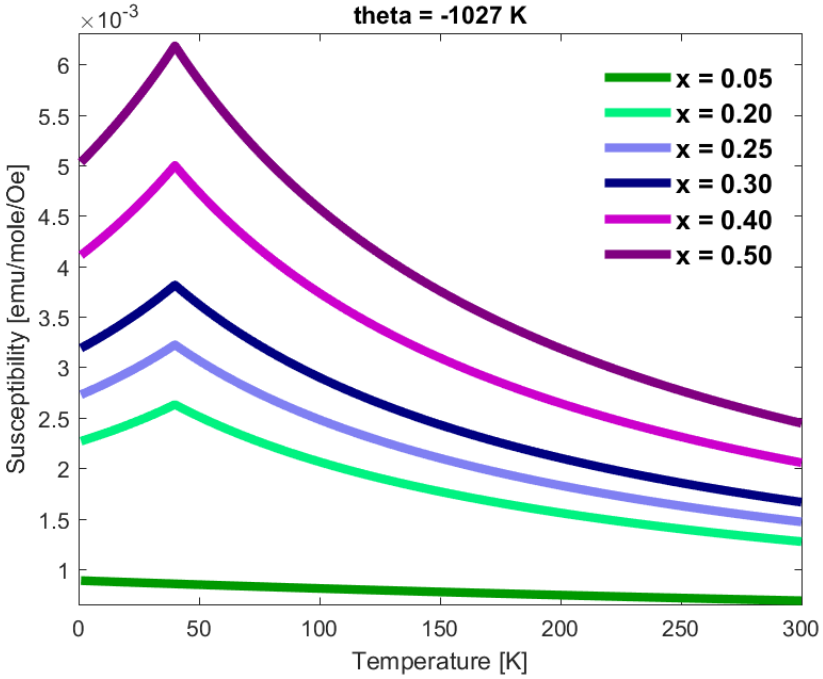

Figure S11. Example showing the susceptibility of a combination of an antiferromagnetic (x = 0.50) and a paramagnetic phase (x = 0.05) coexisting in $LaNi_{1-x}Pt_xO_3$. The data is calculated using the Curie-Weiss relation for both the paramagnetic phase and for the AFM phase (in paramagnetic conditions) above T_N = 40 K. Below T_N in this example (40-0 K), the AFM phase is assumed to have the same susceptibility as from 40-80 K. The magnetic moment and θ shown in Table 1 are used for modelling the susceptibility for both the paramagnetic (m = 2.7 μB, θ = –1027 K) and AFM (m = 2.9 μB, θ = –130 K) phase.

9. References

1. Schwartz, K.B. and Prewitt, C.T., *Structural and electronic properties of binary and ternary platinum oxides.* Journal of Physics and Chemistry of Solids, 1984. **45**(1): p. 1-21.

2. Lee, M.-C., Sohn, C.H., Kim, S.Y., Lee, K.D., Won, C.J., Hur, N., Kim, J.Y., Cho, D.-Y., and Noh, T.W., *Stabilization of ferromagnetic ordering in cobaltite double perovskites of La_2CoIrO_6 and La_2CoPtO_6.* Journal of Physics: Condensed Matter, 2015. **27**(33): p. 336002.
3. Das, H., Sanyal, P., Saha-Dasgupta, T., and Sarma, D.D., *Origin of magnetism and trend in Tc in Cr-based double perovskites: Interplay of two driving mechanisms.* Physical Review B, 2011. **83**(10): p. 104418.
4. Ouchetto, K., Archaimbault, F., Choisnet, J., and Et-Tabirou, M., *New ordered and distorted perovskites: the mixed platinates Ln_2MPtO_6 (Ln = La, Pr, Nd, Sm, Eu, Gd; M = Mg, Co, Ni, Zn).* Mater. Chem. Phys., 1997. **51**(2): p. 117-124.
5. Zhou, J.S., Goodenough, J.B., and Dabrowski, B., *Exchange Interaction in the Insulating Phase of $RNiO_3$.* Physical Review Letters, 2005. **95**(12): p. 127204.
6. Androulakis, J. and Giapintzakis, J., *Magnetoresistance in $LaNi_{1-x}CoxO_3$ (0.3 <= x <= 0.6).* Physica B, 2010. **405**(1): p. 107-112.
7. Schinzer, C., *Spin-glass behavior of disordered perovskite $LaNi_{1/2}Rh_{1/2}O_3$.* J. Alloys Compd., 1999. **288**(1-2): p. 65-75.
8. Battle, P.D. and Vente, J.F., *Structural and Magnetic Characterization of La_2NiRhO_6.* J. Solid State Chem., 1999. **146**(1): p. 163-167.
9. Asai, K., Sekizawa, H., Mizushima, K., and Iida, S., *Magnetic Properties of $LaNi_{1-x}Fe_xO_3$ ($0 \leqslant x \leqslant 0.2$).* Journal of the Physical Society of Japan, 1978. **45**(4): p. 1417-1418.
10. Vasanthacharya, N.Y., Ganguly, P., Goodenough, J.B., and Rao, C.N.R., *Valence states and magnetic properties of $LaNi_{1-x}Mn_xO_3$ (for $0 \leqslant x \leqslant 0.2$ and x = 0.5).* Journal of Physics C: Solid State Physics, 1984. **17**(15): p. 2745-2760.
11. Meneghini, C., Ray, S., Liscio, F., Bardelli, F., Mobilio, S., and Sarma, D.D., *Nature of ``Disorder'' in the Ordered Double Perovskite Sr_2FeMoO_6.* Physical Review Letters, 2009. **103**(4): p. 046403.
12. Sarma, D.D., Ray, S., Tanaka, K., Kobayashi, M., Fujimori, A., Sanyal, P., Krishnamurthy, H.R., and Dasgupta, C., *Intergranular Magnetoresistance in Sr_2FeMoO_6 from a Magnetic Tunnel Barrier Mechanism across Grain Boundaries.* Physical Review Letters, 2007. **98**(15): p. 157205.
13. Topwal, D., Sarma, D.D., Kato, H., Tokura, Y., and Avignon, M., *Structural and magnetic properties of $Sr_2Fe_{1+x}Mo_{1-x}O_6$ ($1 \leqslant x \leqslant 0.25$).* Physical Review B, 2006. **73**(9): p. 094419.
14. Vasala, S. and Karppinen, M., *$A_2B'B''O_6$ perovskites: A review.* Progress in Solid State Chemistry, 2015. **43**(1-2): p. 1-36.
15. Budiman, R.A., Hashimoto, S.i., Nakamura, T., Yashiro, K., Amezawa, K., and Kawada, T., *Oxygen Nonstoichiometry and Electrochemical Properties of LaNiO3-* ECS Transactions, 2015. **66**(2): p. 177-183.
16. van Beek, W., Safonova, O.V., Wiker, G., and Emerich, H., *SNBL, a dedicated beamline for combined in situ X-ray diffraction, X-ray absorption and Raman scattering experiments.* Phase Transitions, 2011. **84**(8): p. 726-732.
17. Dyadkin, V., Pattison, P., Dmitriev, V., and Chernyshov, D., *A new multipurpose diffractometer PILATUS@SNBL.* J Synchrotron Radiat, 2016. **23**(3): p. 825-829.
18. Coelho, A.A., *TOPAS and TOPAS-Academic: an optimization program integrating computer algebra and crystallographic objects written in C++.* Journal of Applied Crystallography, 2018. **51**(1): p. 210-218.
19. Zhou, J.S., Marshall, L.G., and Goodenough, J.B., *Mass enhancement versus Stoner enhancement in strongly correlated metallic perovskites: $LaNiO_3$ and $LaCuO_3$.* Physical Review B, 2014. **89**(24): p. 245138.
20. Tilley, R.J.D., *Understanding solids : the science of materials*. 2nd ed. ed. 2013, Chichester: Wiley.
21. Yan, J.Q., Zhou, J.S., and Goodenough, J.B., *Ferromagnetism in $LaCoO_3$.* Physical Review B, 2004. **70**(1): p. 014402.
22. Zhou, J.S. and Goodenough, J.B., *Chemical bonding and electronic structure of $RNiO_3$, R= rare earth.* Physical Review B, 2004. **69**(15): p. 153105.

23. Fjellvåg, A.S., Fjellvåg, Ø.S., Kumar, S., Ruud, A., and Sjåstad, A.O., *Interplay of valence states and magnetic interactions in the perovskite system LaNi1–xRhxO3.* Journal of Solid State Chemistry, 2021: p. 122124.
24. Karolak, M., Edelmann, M., and Sangiovanni, G., *Nickel-titanium double perovskite: A three-dimensional spin-1 Heisenberg antiferromagnet.* Phys. Rev. B, 2015. **91**(7).
25. Alonso, J.A., García-Muñoz, J.L., Fernández-Díaz, M.T., Aranda, M.A.G., Martínez-Lope, M.J., and Casais, M.T., *Charge Disproportionation in $RNiO_3$ Perovskites: Simultaneous Metal-Insulator and Structural Transition in $YNiO_3$.* Physical Review Letters, 1999. **82**(19): p. 3871-3874.
26. Alonso, J.A., Martínez-Lope, M.J., Casais, M.T., García-Muñoz, J.L., Fernández-Díaz, M.T., and Aranda, M.A.G., *High-temperature structural evolution of $RNiO_3$ (R = Ho, Y, Er, Lu) perovskites: Charge disproportionation and electronic localization.* Physical Review B, 2001. **64**(9): p. 094102.
27. Li, B., Louca, D., Yano, S., Marshall, L.G., Zhou, J., and Goodenough, J.B., *Insulating Pockets in Metallic $LaNiO_3$.* Advanced Electronic Materials, 2016. **2**(2): p. 1500261.